Comparison of through-space homonuclear correlations between quadrupolar nuclei in solids

Jennifer S. Gómez, Julien Trebosc, Nghia Tuan Duong, Frederique Pourpoint, Olivier Lafon, Jean-Paul Amoureux

To cite this version:

Jennifer S. Gómez, Julien Trebosc, Nghia Tuan Duong, Frederique Pourpoint, Olivier Lafon, et al.. Comparison of through-space homonuclear correlations between quadrupolar nuclei in solids. Journal of Magnetic Resonance, 2023, Journal of Magnetic Resonance, 348, pp.107388. 10.1016/j.jmr.2023.107388 . hal-04095767

HAL Id: hal-04095767
https://hal.univ-lille.fr/hal-04095767v1

Submitted on 21 Nov 2023

Comparison of through-space homonuclear correlations between quadrupolar nuclei in solids

Jennifer S. Gómez,[1] Julien Trébosc,[2] Nghia Tuan Duong,[3#] Frédérique Pourpoint,[1] Olivier Lafon,[1*] Jean-Paul Amoureux[1,4*]

[1] Univ. Lille, CNRS, Centrale Lille, Univ. Artois, UMR 8181 – UCCS – Unité de Catalyse et Chimie du Solide, Lille, 59000, France.
[2] Univ. Lille, CNRS, INRAE, Centrale Lille, Univ. Artois, FR 2638 – IMEC – Fédération Chevreul, Lille, 59000, France.
[3] Nano-Crystallography Unit, RIKEN-JEOL Collaboration Center, Yokohama, Kanagawa 230-0045, Japan.
[4] Bruker Biospin, 34 rue de l'industrie, Wissembourg, 67166, France.
[#] Present address: Aix Marseille Univ, CNRS, ICR, 13397 Marseille, France.

Correspondance to: Olivier Lafon: olivier.lafon@univ-lille.fr

Jean-Paul Amoureux: jean-paul.amoureux@univ-lille.fr

Keywords. homonuclear correlation, quadrupolar nuclei, spatial proximity, double-quantum coherences, single-quantum coherences.

ABSTRACT. Various two-dimensional (2D) homonuclear correlation experiments have been proposed to observe proximities between identical half-integer spin quadrupolar nuclei in solids. These experiments select either the single- or double-quantum coherences during the indirect evolution period, t_1. We compare here the efficiency and the robustness of the 2D double-quantum to single-quantum (DQ-SQ) and SQ-SQ homonuclear correlations for two half-integer spin quadrupolar isotopes subject to small chemical shift anisotropy (CSA): ^{11}B with a nuclear spin $I = 3/2$ and ^{27}Al with $I = 5/2$. Such a comparison is performed using experiments on two model samples: $Li_2B_4O_7$ for ^{11}B and $AlPO_4$-14 for ^{27}Al. For both isotopes, the DQ-SQ homonuclear correlations are recommended since they allow probing the proximities between nuclei with close or identical frequencies. In the case of small or moderate isotropic chemical shift differences (e.g. ^{11}B) the $[SR2_2^1]$ or $[BR2_2^1]$ bracketed DQ-SQ recoupling schemes are recommended; whereas it is the $BR2_2^1$ un-bracketed one otherwise (e.g. ^{27}Al).

I. Introduction

Half-integer spin quadrupolar nuclei, such as ^{11}B with spin $I = 3/2$, or ^{17}O and ^{27}Al with $I = 5/2$, represent more than 66% of isotopes detectable by NMR [1]. However, the observation of proximities between identical half-integer spin quadrupolar nuclei is more challenging than between identical spin-1/2 isotopes since quadrupolar nuclei (i) have a higher number of energy levels, equal to $(2I + 1)$, leading to a larger size of the density matrix, and (ii) are subject to the quadrupolar interaction, which is an anisotropic NMR interaction with a magnitude much larger than the radiofrequency (rf) field and the magic-angle spinning (MAS) frequency. Therefore, the spin dynamics of quadrupolar nuclei is more complicated than that of spin-1/2 isotopes under MAS and rf-field irradiation. As a result, proximities between identical half-integer spin quadrupolar nuclei have been initially probed without the application of rf-field [2–8]. These approaches rely on (i) rotational resonance (R^2) [8], (ii) cross-terms between dipolar interactions between the nuclei and their first-order quadrupolar interaction [4–7], or (iii) their heteronuclear dipolar couplings with protons [2,3]. However, the efficiency of these recoupling approaches is often small and it strongly depends on the MAS frequency, the internal spin interactions and the presence of protons.

To circumvent these issues, homonuclear dipolar couplings between half-integer spin quadrupolar nuclei have been reintroduced using rf irradiation of the central transition (CT) between energy levels $m_I = -1/2$ and $+1/2$, which is not subject to first-order quadrupolar interaction [9–21]. Initially, continuous rf irradiation relying on the rotary resonance recoupling (R^3) has been employed [9–11]. In particular, the homonuclear rotary recoupling (HORROR) [12], for which the nutation frequency of the CT, $\nu_{CT} = (I + 1/2)\nu_1$, is equal to half of the MAS frequency, ν_R,

$$\nu_1 = \nu_R/(2I + 1) \quad (1)$$

This recoupling is advantageous since it employs a weak rf-field, which limits the excitation of the satellite transitions (STs, $m_I \leftrightarrow m_I - 1$ with $m_I \neq 1/2$) and the related losses. However, this weak rf-field leads to a high sensitivity to the carrier frequency, and moreover the HORROR condition is highly sensitive to the rf-field amplitude. Therefore, multi-pulse recoupling schemes using the same rf-field amplitude, including $\mathrm{SR4}_4^1$ and $\mathrm{SR2}_n^1 = \mathrm{R2}_n^1\mathrm{R2}_n^{-1}$ with $n = 2$ or 4 and $\mathrm{BR2}_2^1$ sequences, were introduced to improve the robustness to offset and rf-field inhomogeneity [13–21]. These recoupling schemes reintroduce the double-quantum (DQ) operators and hence, can be employed to excite and reconvert the DQ coherences between distinct quadrupolar nuclei in two-dimensional (2D) correlations between DQ and single-quantum (SQ) coherences. Recently, symmetry-based sequences using the same rf-field amplitude, such as $(\mathrm{SR2}_2^1)_4$, $(\mathrm{SR2}_4^1)_4$ and $(\mathrm{SR2}_8^1)_4$, have been proposed to correlate the SQ coherences of distinct CTs [17,18].

We compare here the performances of 2D SQ-SQ and DQ-SQ through-space homonuclear correlation (*D*-HOMCOR) experiments for two half-integer spin isotopes subject to small chemical shift anisotropy (CSA): ^{11}B with $I = 3/2$ and ^{27}Al with $I = 5/2$. This comparison is carried out on two model samples: $Li_2B_4O_7$ for ^{11}B and $AlPO_4$-14 for ^{27}Al.

II. Theory and pulse sequences

II-1. Dipolar recoupling

The $\mathrm{SR4}_4^1$ and $\mathrm{SR2}_n^1$ sequences with $n = 2$, 4 or 8, which have been identified as the most efficient symmetry-based dipolar recoupling between half-integer quadrupolar nuclei [14,15,17,18,20,21], are displayed in Fig.1. The $\mathrm{SR2}_2^1$ and $\mathrm{SR4}_4^1$ recouplings employ single 180° square-pulse, whereas the $\mathrm{SR2}_4^1$ and $\mathrm{SR2}_8^1$ variants are built from composite inversion pulses, 90_0270_{180} and $360_{180}270_090_{180}$, respectively, where ξ_θ denotes a CT-selective pulse with flip-angle ξ and phase θ. The $\mathrm{SR4}_4^1$ and $\mathrm{SR2}_n^1$ sequences employ a phase inversion supercycle to improve their robustness.

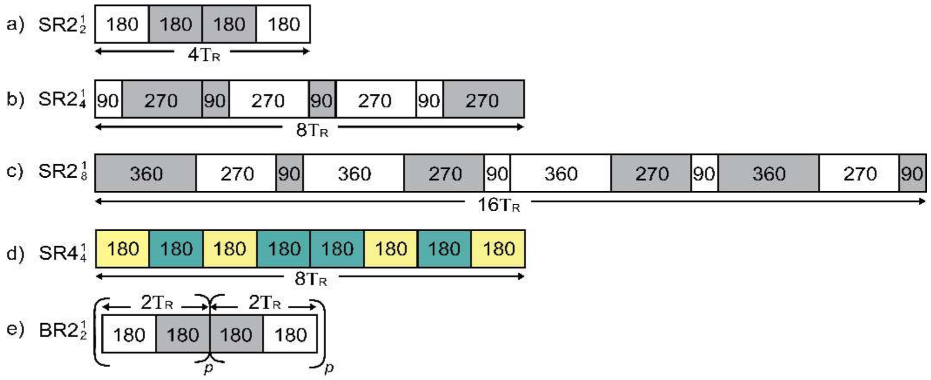

Fig.1. (a) $\mathrm{SR2}_2^1$, (b) $\mathrm{SR2}_4^1$, (c) $\mathrm{SR2}_8^1$, (d) $\mathrm{SR4}_4^1$, and (e) $\mathrm{BR2}_2^1$ homonuclear dipolar recoupling schemes. In (a-c,e), the pulses with phase of 0 and 180° are displayed as white and grey rectangles, respectively, whereas in (d) the pulses with phases of 45° and 315° are displayed as yellow and green colors. In all cases, the integer number indicated in each square is the ξ flip-angle of the CT-selective pulse.

The $\mathrm{SR2}_n^1$ and $\mathrm{SR4}_4^1$ schemes shown in Fig.1a-d are periodic, and the contribution of the homonuclear dipolar coupling to the average Hamiltonian (AH) is [14,20]

$$H_S^{jk} = \kappa b_{jk} * f(2\beta_{jk},\gamma_{jk})\{I_j^+I_k^+ + I_j^-I_k^- + I_j^+I_k^- + I_j^-I_k^+ - 4I_{jz}I_{kz}\}/2 \quad (2)$$

where $\kappa = 3/(8\sqrt{2}) \approx 0.265$ is the dipolar scaling factor, b_{jk} is the dipolar coupling constant in rad.s^{-1}, $f(2\beta_{jk},\gamma_{jk}) = \sin(2\beta_{jk})\cos(\gamma_{jk})$, where (β_{jk},γ_{jk}) are the Euler angles relating the $\boldsymbol{r}_{jk}$ inter-nuclear vector to the MAS rotor-fixed frame, $I_j^\pm$ and $I_k^\pm$ are the ladder operators of the spins j and k. The Hamiltonian of Eq.2 contains $\left(I_j^+ I_k^+ + I_j^- I_k^-\right)$, which is a DQ operator, as well as $\left(I_j^+ I_k^- + I_j^- I_k^+ - 4 I_{jz} I_{kz}\right)$, which is a zero-quantum (ZQ) operator. This recoupling is non-γ-encoded since the norm of the Hamiltonian depends on γ_{jk} as seen in Eq.2 [22,23].

The DQ and ZQ operators can interfere leading to a decreased efficiency. The DQ operator can be removed in Eq.2 using an M-quantum phase cycles, denoted $(\mathrm{SR}2_{\mathrm{n}}^{1})_{\mathrm{M}}$, with $M \geq 3$, which consists of M successive $\mathrm{SR}2_{\mathrm{n}}^{1}$ blocks with an overall phase shift of 360°/M between consecutive blocks. It has been reported that quadruple-quantum phase cycle employing phase shift of 90° performs slightly better than its triple-quantum counterpart [17]. After this supercycling, the contribution of the homonuclear dipolar coupling to the AH only contains the ZQ operator:

$$H_{S(M\geq 3)}^{jk} = \kappa b_{jk} * f\left(2\beta_{jk}, \gamma_{jk}\right)\left\{I_j^+ I_k^- + I_j^- I_k^+ - 4 I_{jz} I_{kz}\right\}/2 \tag{3}$$

The $\mathrm{SR}2_{\mathrm{n}}^{1}$ and $\mathrm{SR}4_{4}^{1}$ sequences can also be bracketed by 90° CT-selective pulses to convert the ZQ operators into DQ ones. These bracketed recoupling schemes are denoted $[\mathrm{SR}2_{\mathrm{n}}^{1}]$ and $[\mathrm{SR}4_{4}^{1}]$ hereafter. The homonuclear dipolar term in their AH is equal to

$$H_{[S]}^{jk} = \kappa b_{jk} * f\left(2\beta_{jk}, \gamma_{jk}\right)\left\{ I_j^+ I_k^+ + I_j^- I_k^- \right\} \tag{4}$$

The build-up of DQ coherences between distinct CTs is twice faster during $[\mathrm{SR}2_{\mathrm{n}}^{1}]$ and $[\mathrm{SR}4_{4}^{1}]$ than their unbracketed variants.

The $\mathrm{BR}2_{2}^{1}$ scheme shown in Fig.1e corresponds to the sequence $(\mathrm{R}2_{2}^{1})_{\mathrm{p}}(\mathrm{R}2_{2}^{-1})_{\mathrm{p}}$ built from single 180° pulses, where p is the number of loops. It employs a phase inversion at the midpoint of the recoupling delay, $\tau_{\mathrm{mix}} = 4pT_{\mathrm{R}}$, which was initially employed for the HORROR scheme [12]. This sequence is not periodic, which prevents the straightforward application of AH theory [19,21]. Nevertheless, using a Magnus expansion, an effective Hamiltonian for the $\mathrm{BR}2_{2}^{1}$ scheme can be derived in the offset-toggling frame and is equal to [19]

$$\begin{aligned} H_{\mathrm{BR}2_{2}^{1}}^{jk} = \kappa b_{jk} * f\left(2\beta_{jk}, \gamma_{jk}\right)\Big\{&\left(1 - \tfrac{1}{2}[S(\Delta) - S(\Sigma)]\right)\left(I_j^+ I_k^- + I_k^+ I_j^-\right) - [S(\Delta) + S(\Sigma)] 2 I_{jz} I_{kz} \\ &+ [C(\Sigma) + C(\Delta)] 2 I_{jy} I_{kz} + [C(\Sigma) - C(\Delta)] 2 I_{jz} I_{ky} \\ &+ \left(1 + \tfrac{1}{2}[S(\Delta) - S(\Sigma)]\right)\left(I_j^+ I_k^+ + I_j^- I_k^-\right)\Big\}/2 \end{aligned} \tag{5}$$

where $S(\Psi) = \sin(8\mathrm{p}\Psi\mathrm{T}_{\mathrm{R}})/(8\mathrm{p}\Psi\mathrm{T}_{\mathrm{R}})$ and $C(\Psi) = \{\cos(8\mathrm{p}\Psi\mathrm{T}_{\mathrm{R}})/(8\mathrm{p}\Psi\mathrm{T}_{\mathrm{R}}) - 1\}$, with $\Psi = \Sigma$ or Δ, the sum and difference of isotropic shifts for nuclei j and k. This Hamiltonian contains ZQ ($I_{jz} I_{kz}$ and $I_j^+ I_k^- + I_k^+ I_j^-$), SQ ($I_{jy} I_{kz}$ and $I_{jz} I_{ky}$) as well as DQ ($I_j^+ I_k^+ + I_j^- I_k^-$) operators. It depends on the length of the $\mathrm{BR}2_{2}^{1}$ recoupling, $\tau_{\mathrm{mix}} = 4pT_{\mathrm{R}}$, but also on Σ and Δ, and hence, on the offset values. In the case of two distinct resonances ($\Delta \neq 0$), which are not irradiated in the middle ($\Sigma \neq 0$), the functions $S(\Psi)$ and $C(\Psi)$ are close to 0 for long recoupling, $4pT_{\mathrm{R}} \gg 1/(2\Delta)$ and $1/(2\Sigma)$, and the effective $\mathrm{BR}2_{2}^{1}$ Hamiltonian simplifies into

$$H_{BR2_{2}^{1}}^{jk} \approx \kappa b_{jk} * f\left(2\beta_{jk}, \gamma_{jk}\right)\left\{\left(I_j^+ I_k^- + I_k^+ I_j^-\right) + \left(I_j^+ I_k^+ + I_j^- I_k^-\right)\right\}/2 \tag{6}$$

The same coefficient for the DQ operator is obtained for any recoupling time in the case of on-resonance irradiation of one of the two resonances, *i.e.* $\Sigma = \pm\Delta$, whereas in the case of long recoupling, this coefficient is 50% lower when irradiating the middle of two distinct resonance frequencies ($\Sigma = 0$ and $\Delta \neq 0$) and 50% higher for the off-resonance irradiation of an autocorrelation peak ($\Sigma \neq 0$ and $\Delta = 0$). Therefore, the build-up of DQ coherences during the $\mathrm{BR}2_{2}^{1}$ sequence depends on the offset values.

In the present article, we also employ the $[\mathrm{BR}2_{2}^{1}]$ recoupling, in which the $\mathrm{BR}2_{2}^{1}$ sequence is bracketed by two 90° CT selective pulses with phases shifted by 90° with respect the 180° pulse of the $\mathrm{BR}2_{2}^{1}$ sequence. Its effective Hamiltonian can be derived from Eq.5 and is equal to

$$\begin{aligned} H_{[\mathrm{BR}2_{2}^{1}]}^{jk} = \kappa b_{jk} * f\left(2\beta_{jk}, \gamma_{jk}\right)\Big\{&\left(1 - \tfrac{1}{2}[S(\Delta) + S(\Sigma)]\right)\left(I_j^+ I_k^- + I_k^+ I_j^-\right) - [S(\Delta) - S(\Sigma)] 2 I_{jz} I_{kz} \\ &+ [C(\Sigma) + C(\Delta)] 2 I_{jz} I_{ky} + [C(\Sigma) - C(\Delta)] 2 I_{jy} I_{kz} \\ &+ \left(1 + \tfrac{1}{2}[S(\Delta) + S(\Sigma)]\right)\left(I_j^+ I_k^+ + I_j^- I_k^-\right)\Big\}/2\,. \end{aligned} \tag{7}$$

Hence, contrary to $[\mathrm{SR}2_n^1]$ and $[\mathrm{SR}4_4^1]$, the effective $[\mathrm{BR}2_2^1]$ Hamiltonian recoupling also contains ZQ, SQ and DQ operators, like that of the $\mathrm{BR}2_2^1$ scheme. Nevertheless, for the on-resonance irradiation of an autocorrelation peak, *i.e.* $\Delta = \Sigma = 0$, the effective Hamiltonian of the $[\mathrm{BR}2_2^1]$ scheme simplifies into Eq.4 and the scaling factor of the DQ operator is two-fold higher than that of $\mathrm{BR}2_2^1$ under the same conditions, which results in faster build-up of DQ coherences. When irradiating the middle of two distinct resonance frequencies ($\Sigma = 0$ and $\Delta \neq 0$), the coefficient of the DQ operator for a long $[\mathrm{BR}2_2^1]$ recoupling is reduced by 50%, but remains three-fold higher than for $\mathrm{BR}2_2^1$. Hence, the $[\mathrm{BR}2_2^1]$ scheme still benefits from faster build-up of DQ coherences. Conversely, the same coefficient of the DQ operator is obtained for the off-resonance irradiation of the autocorrelation peak ($\Sigma \neq 0$ and $\Delta = 0$). In that case, $[\mathrm{BR}2_2^1]$ and $\mathrm{BR}2_2^1$ recouplings produce similar build-up of DQ coherences.

It is important to remind here that the mathematical descriptions made in this section, are based on the RN_n^ν schemes, which follow symmetry considerations not accounting for the quadrupolar interactions, which are often much larger than the rf-field. Therefore, it is difficult to foresee in advance their advantages and limitations; and only the experimental results allow a real comparison between them.

II-2. 2D through-space homonuclear correlations

As mentioned in the introduction, the proximities between half-integer spin quadrupolar nuclei have been probed using either 2D through-space SQ-SQ or DQ-SQ *D*-HOMCOR experiments.

The SQ-SQ variant shown in Fig.**2a** is identical to the NOESY sequence. The first CT-selective 90° pulse excites the SQ coherences, which evolve during the t_1 delay. The second 90° pulse stores the magnetization related to the CTs along the $\boldsymbol{B}_0$ field direction during the mixing time, τ_{mix}, during which a ZQ recoupling, such as $(\mathrm{SR}2_n^1)_4$, exchanges the magnetization between the different spins. The last 90° pulse converts the longitudinal magnetization related to CTs into a transverse magnetization, which is detected during the acquisition period, t_2.

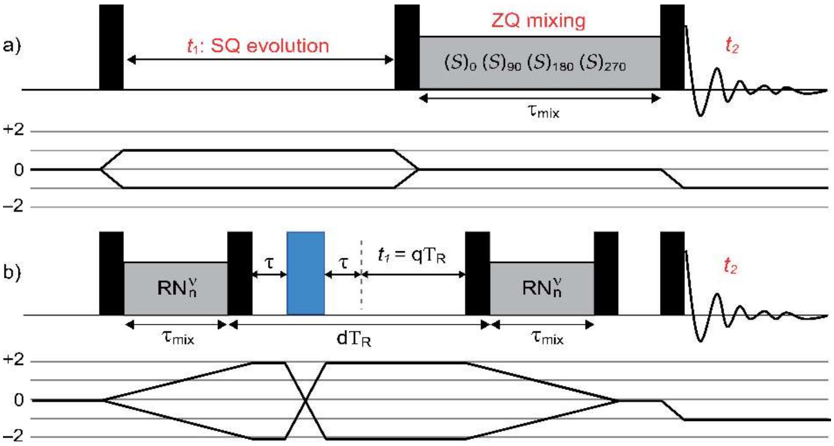

Fig.2. Pulse sequences used for 2D through-space (a) SQ-SQ and (b) DQ-SQ *D*-HOMCOR experiments between half-integer spin quadrupolar nuclei along with their coherence transfer pathways. All pulses are CT-selective with $\nu_1 \approx \nu_R/(2I + 1)$. The 90° and 180° pulses are displayed as black and blue rectangles, respectively. In (a), (S) denotes a $\mathrm{SR}2_n^1$ recoupling displayed in Fig.1a-c. In (b), d and q are integer numbers, and a $[\mathrm{RN}_n^\nu]$ bracketed recoupling is then employed. In the case of an un-bracketed recoupling, only the last reading $\pi/2$-pulse is used. The RN_n^ν recoupling blocks are represented as grey rectangles.

The DQ-SQ technique allows the observation of proximities between nuclei with close or identical resonance frequencies, contrary to SQ-SQ correlations. The DQ-SQ sequence is shown in Fig.**2b** and it employs a DQ dipolar recoupling scheme, such as $\mathrm{SR}2_n^1$, $[\mathrm{SR}2_n^1]$, $\mathrm{BR}2_2^1$ and $[\mathrm{BR}2_2^1]$. The first recoupling block converts the longitudinal magnetization into DQ coherences, which evolve during the t_1 period. The second recoupling block reconverts these coherences into longitudinal magnetizations, which are transferred into CT transverse magnetizations by the last $\pi/2$ reading pulse. Signals passing through DQ coherences are selected using a four-step phase cycle of the initial recoupling scheme. Furthermore, a CT-selective π-pulse (in blue) is applied just before the t_1 period and the $\pm 2\mathrm{Q} \rightarrow \mp 2\mathrm{Q}$ coherence transfer pathways are selected using an eight step phase cycle to only keep the DQ coherences between CTs of distinct nuclei and to remove those between energy levels m_I and $m_I + 2$ of a single nucleus [12]. This π-pulse is bracketed by two identical τ delays to cancel all DQ dephasing. To limit the losses, the τ value should be as small as possible, and thus equal to $(T_R - \tau_{180} - \tau_{90})/2$ or $(T_R - \tau_{180}\}/2$, for bracketed or unbracked recoupling, respectively [24]. As the employed dipolar recouplings are non-γ-encoded, the starts of the excitation and reconversion blocks must be separated by an integer number of rotor periods. As a result, the delay between the end of the first and the beginning of the second recoupling parts must also be rotor-synchronized. The t_1 period is also often rotor-synchronized, $t_1 = qT_R$, to fold back all sidebands along F_1 onto the center-band, which simplifies the spectrum and enhances the sensitivity. The spinning speed may not be sufficient for the frequency spread along F_1, which is the double of that along F_2. In that case, the position of the π-pulse should be changed to decrease the required indirect spectral-width by redistributing the evolution time before and after this pulse [24].

III. NMR experiments

III-1. Samples and experimental section

Crystalline $Li_2B_4O_7$ was synthetized using the procedure detailed in the Supporting Information, whereas $AlPO_4$-14 was prepared as described in ref. [25].

All experiments were recorded on Bruker AVANCE NEO spectrometers operating at B_0 = 9.4 and 18.8 T, with 3.2 mm MAS probes at ν_R = 20 kHz. However, we only present the spectra obtained at 18.8 T, with a HX MAS probe, since this high field scales by 16 the 2D resolution and doubles the required spectral width and hence, is more demanding in term of robustness to offset. The 2D ^{11}B and ^{27}Al SQ-SQ and DQ-SQ *D*-HOMCOR spectra were acquired using the pulse sequences shown in Fig.2a and 2b, respectively. For the SQ-SQ variant, we employed as ZQ recoupling $(\mathrm{SR2}_2^1)_4$, $(\mathrm{SR2}_4^1)_4$ or $(\mathrm{SR2}_8^1)_4$ for ^{11}B nuclei and $(\mathrm{SR2}_2^1)_4$ and $(\mathrm{SR2}_4^1)_4$ for ^{27}Al isotope. For DQ-SQ experiments, the employed recoupling schemes were $\mathrm{SR2}_2^1$, $[\mathrm{SR2}_2^1]$, $\mathrm{BR2}_2^1$ and $[\mathrm{BR2}_2^1]$ for ^{11}B and $\mathrm{BR2}_2^1$ and $[\mathrm{BR2}_2^1]$ for ^{27}Al. The rf field amplitude of the CT-selective π/2 and π pulses, which do not belong to the recoupling blocks, was equal to ca. 5 kHz for ^{11}B and ^{27}Al. To reduce the experimental time, the 2D spectra were acquired using non-uniform sampling (NUS) along the indirect dimension with an exponentially biased sampling [26,27]. ^{11}B isotropic chemical shifts were referenced to $(C_2H_5)_2O{\cdot}BF_3$ (0 ppm) using solid $NaBH_4$ ($\delta_{iso} = -42.05$ ppm) as a secondary reference, whereas ^{27}Al isotropic chemical shifts were referenced to 1 mol.L^{-1} $[Al(H_2O)_6]^{3+}$ solution. Other experimental parameters are given in the figure captions.

IV.1. ^{11}B homonuclear correlations

^{11}B is a spin-3/2 isotope with a natural abundance of 80 % and a Larmor frequency of ν_0 = 256.8 MHz at 18.8 T. Borate materials contain tri- (BO_3) and tetra-coordinated (BO_4) B sites, denoted B^{III} and B^{IV} hereafter. At 18.8 T, the difference in isotropic chemical shifts between these sites do not exceed 5 kHz. We investigated herein crystalline $Li_2B_4O_7$ as a model sample, for which the chemical shift separation between B^{III} and B^{IV} signals is approximately equal to $\Delta \approx 4.2$ kHz at 18.8 T [28]. The quantitative 1D MAS and 2D MQMAS spectra of this sample are shown in Fig. S4 and S5. These spectra are dominated by the B_1^{III} and B^{IV} signals assigned to B^{III} and B^{IV} sites of $Li_2B_4O_7$ phase. The 2D ^{11}B MQMAS spectrum shows the presence of an additional B^{III} signal, denoted B_2^{III}, which is assigned to α-$LiBO_2$ impurity based on the analysis of X-ray diffraction pattern [29–31]. The simulation of the quantitative 1D ^{11}B spectrum shown in Fig.S4 indicates that the integrated intensity of the B_2^{III} signal amounts to 10% of the total integrated intensity and that the NMR parameters of B_1^{III}, B_2^{III} and B^{IV} sites are (δ_{iso} (ppm), C_Q (MHz), η_Q) = (18.4, 2.63, 0.18), (16.5, 2.36, 0.60) and (2.1, 0.48, 0.51), respectively.

It must be noted that the two B^{III} resonances are narrow and well separated in the MQMAS spectrum (Fig.S5), which means that the two different compounds ($Li_2B_4O_7$ and α-$LiBO_2$) are well-crystallised and thus phase separated in the sample, hence leading to the lack of spatial proximity between the B_2^{III} species and the B_1^{III} and B^{IV} ones.

In the following, the two B_1^{III} and B_2^{III} resonances are considered as a single one, and the sample will be called $Li_2B_4O_7$, neglecting the α-$LiBO_2$ impurity. We will call B^3 and B^4 the auto-correlation peaks of ($B_1^{III} + B_2^{III}$) and B^{IV} species, and B^{34} and B^{43} the cross-peaks observed along the F_2 dimension at (B_1^{III} + B_2^{III}) and B^{IV} frequencies, respectively.

IV.1.a. SQ-SQ

Figure 3 shows the 2D ^{11}B SQ-SQ *D*-HOMCOR spectra of $\mathrm{Li_2B_4O_7}$ sample acquired using $(\mathrm{SR}2^{1}_{2})_4$, $(\mathrm{SR}2^{1}_{4})_4$ and $(\mathrm{SR}2^{1}_{8})_4$ recouplings for a given offset and different recoupling times. These spectra are dominated by uninformative diagonal peaks, B^3 and B^4, which subsume the contributions of magnetization that has not been transferred and magnetization transferred between nuclei with identical resonance frequencies. The spectra obtained using $(\mathrm{SR}2^{1}_{2})_4$ exhibits two cross-peaks B^{34} and B^{43}. These cross-peaks stem from the transfer of magnetization between $\mathrm{B}_1^{\mathrm{III}}$ and B^{IV} sites in $\mathrm{Li_2B_4O_7}$ phase. According to the crystal structure (Fig.S2), the closest distance between these sites is equal to 2.46 Å, which corresponds to a ^{11}B-^{11}B dipolar coupling constant of 848 Hz. The intensity of the B^{43} cross-peak is always smaller than that of the B^{34} one since the $^{11}\mathrm{B}_1^{\mathrm{III}}$ nuclei, which are subject to a larger quadrupolar interaction than $^{11}\mathrm{B}^{\mathrm{IV}}$ sites, exhibit a faster decay of their SQ coherences. Furthermore, for $(\mathrm{SR}2^{1}_{4})_4$ and $(\mathrm{SR}2^{1}_{8})_4$ recouplings, the intensities of these cross-peaks is reduced. In particular, the B^{43} peak is not detected for both sequences, whereas the B^{34} one is negative for $(\mathrm{SR}2^{1}_{8})_4$. The comparison of the 1D slices shown in Figure **5a**,**c**,**e** indicates that $(\mathrm{SR}2^{1}_{2})_4$ produces twice more intense B^{34} cross-peaks than the other recoupling schemes, which is consistent with the numerical simulations for diborate unit shown in Fig.S7.

It must be noted that at ν_R = 20 kHz the mixing step of these $(\mathrm{SR}2^{1}_{n})_4$ sequences is long: $\Delta\tau_{\mathrm{mix}} = 8nT_R$ = 0.8, 1.6 and 3.2 ms with n = 2, 4 and 8, respectively.

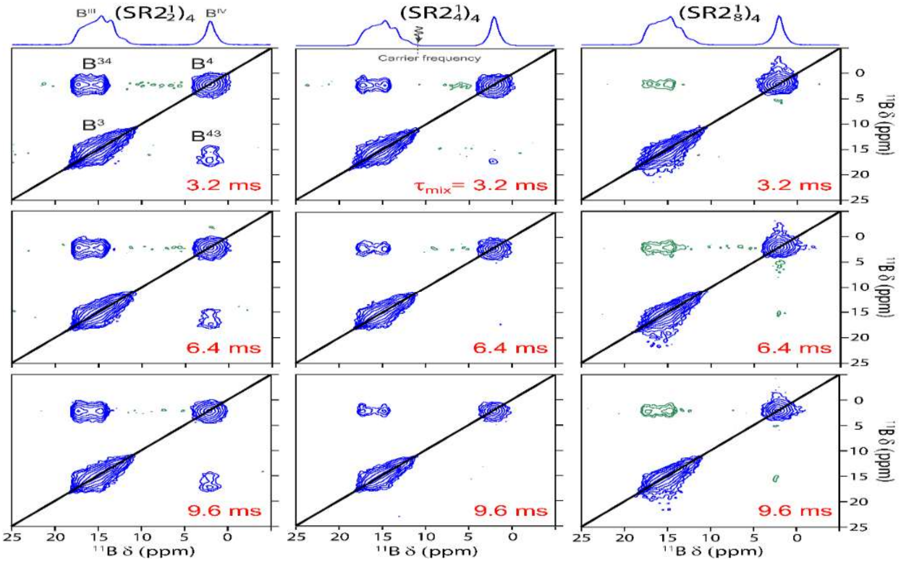

Fig.3. 2D ^{11}B SQ-SQ *D*-HOMCOR spectra of $\mathrm{Li_2B_4O_7}$ acquired at 18.8 T with ν_R = 20 kHz using $(\mathrm{SR}2^{1}_{2})_4$ (first column), $(\mathrm{SR}2^{1}_{4})_4$ (second column) and $(\mathrm{SR}2^{1}_{8})_4$ (third column) ZQ recoupling schemes recorded with τ_{mix} = 3.2 (first line), 6.4 (second line) or 9.6 ms (third line) and an optimized offset value ν_{offset} = 3 kHz (11.7 ppm) indicated by an arrow in the top middle spectrum. These spectra were acquired using NUS retaining 50% of the points with respect to uniform sampling [26,27]. The negative cross-peaks are shown in green. Each 2D spectrum results from averaging NS = 48 transients for each of N_1 = 120 t_1-increment with a recovery delay τ_{RD} = 1 s, yielding an experimental time $T_{\mathrm{exp}} \approx$ 48 min.

Figure 4 shows the 2D ^{11}B SQ-SQ *D*-HOMCOR spectra of the same sample acquired using the same ZQ recouplings for three different offset values. For each offset, the τ_{mix} value was optimized to maximize the intensity of the B^{34} cross-peak. As already noticed in Fig.3, $(\mathrm{SR}2^{1}_{2})_4$ recoupling produces the most intense B^{43} cross-peak, whereas they are hardly visible for $(\mathrm{SR}2^{1}_{4})_4$ and not detected for $(\mathrm{SR}2^{1}_{8})_4$. Furthermore, the 1D slices corresponding to B^{34} cross-peaks shown in Fig.**5b**,**d**,**f** show also that for all offset, $(\mathrm{SR}2^{1}_{2})_4$ recoupling yields the most intense cross-peaks.

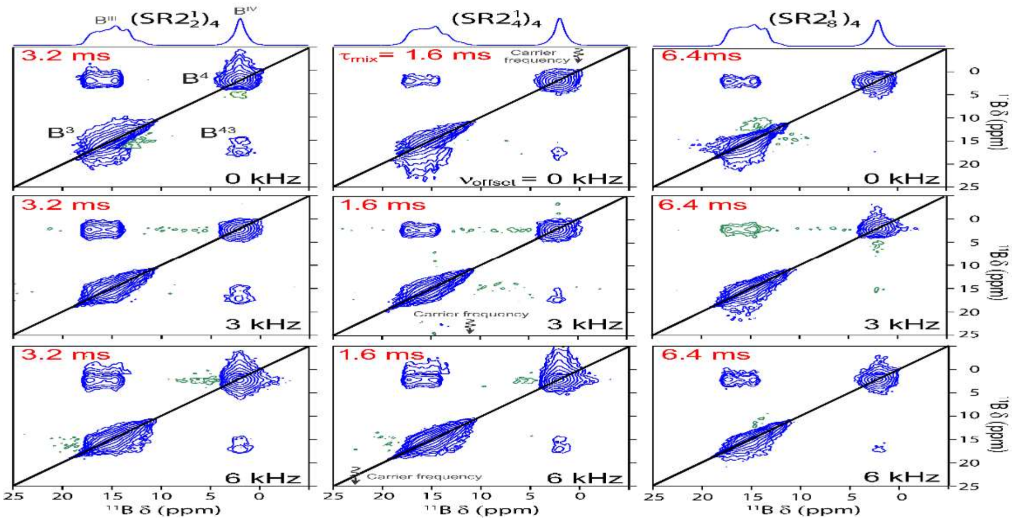

Fig.4. 2D ^{11}B SQ-SQ *D*-HOMCOR spectra of $Li_2B_4O_7$ acquired at 18.8 T with ν_R = 20 kHz using $(\mathrm{SR}2^1_2)_4$ (first column), $(\mathrm{SR}2^1_4)_4$ (second column) and $(\mathrm{SR}2^1_8)_4$ (third column) ZQ recoupling schemes recorded with carrier frequency at ν_{offset} = 0 (first line), 3 (second line) and 6 kHz (third line). The τ_{mix} delay is equal 3.2, 1.6 or 6.4 ms for $(\mathrm{SR}2^1_2)_4$, $(\mathrm{SR}2^1_4)_4$ and $(\mathrm{SR}2^1_8)_4$ recouplings and an optimized offset value (0, 3, 6 kHz) indicated by an arrow in the middle column spectra. The other experimental parameters are identical to those given in the caption of Fig.3. The negative cross-peaks are shown in green.

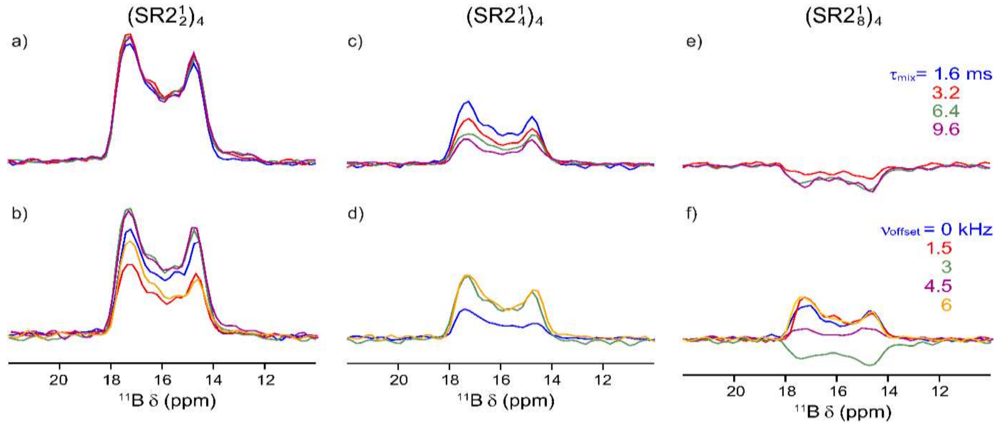

Fig.5. 1D slices along the F_2 dimension corresponding to the B^{34} cross-peak of ^{11}B SQ-SQ *D*-HOMCOR spectra of $Li_2B_4O_7$ shown in Figures 3 and 4 acquired at 18.8 T with ν_R = 20 kHz using $(\mathrm{SR}2^1_2)_4$ (first column), $(\mathrm{SR}2^1_4)_4$ (second column) and $(\mathrm{SR}2^1_8)_4$ (third column) and (a,c,e) ν_{offset} = 3 kHz and τ_{mix} = 1.6, 3.2, 6.4, 9.6 ms as well as (b,d,f) ν_{offset} = 0, 1.5, 3, 4.5, 6 kHz and τ_{mix} = (b) 3.2, (d) 1.6 and (f) 6.4 ms.

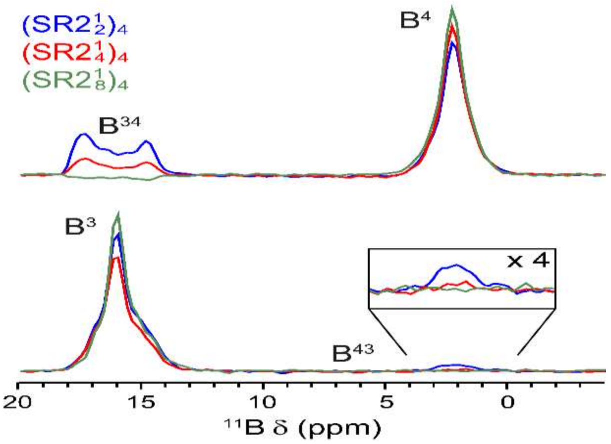

Fig.6. 1D slices along the F_2 dimension corresponding to the B^4 diagonal peak and B^{34} cross-peak (top) and B^3 diagonal peak and B^{43} cross-peak (bottom) of 2D ^{11}B SQ-SQ *D*-HOMCOR spectra of $Li_2B_4O_7$ shown in Figure 3 acquired at 18.8 T with ν_R = 20 kHz using $(\mathrm{SR}2^1_2)_4$ (blue), $(\mathrm{SR}2^1_4)_4$ (red) and $(\mathrm{SR}2^1_8)_4$ (green), with ν_{offset} = 3 kHz (11.7 ppm) and τ_{mix} = 3.2 ms.

Nevertheless, even in the case of the $(\mathrm{SR}2_2^1)_4$ recoupling, the intensity of the cross-peaks remains small with respect to the diagonal peaks, as seen in Fig.6. Therefore, the diagonal peaks can mask cross-peaks between nuclei with close resonance frequencies. Furthermore, the intensity of the diagonal peaks is dominated by the magnetization that has not been transferred. As a result, the magnetization transfer in the SQ-SQ variant cannot be optimized by acquiring 1D spectra corresponding to the first row of the 2D experiment, *i.e.* $t_1 = 0$.

IV.1.b. DQ-SQ

Following Edén's conclusions [17,18,20,21], we have compared the efficiency and robustness of the 2D ^{11}B DQ-SQ *D*-HOMCOR experiments using $\mathrm{SR}2_2^1$, $[\mathrm{SR}2_2^1]$, $\mathrm{BR}2_2^1$ and $[\mathrm{BR}2_2^1]$ recouplings. An advantage of the DQ-SQ variant over its SQ-SQ counterpart is that the magnetization that is not transferred is eliminated by the phase cycling and the transfer can be easily optimized by recording 1D spectra corresponding to the first row ($t_1 = 0$) of the 2D experiment. As expected, the build-up of DQ coherences is faster for bracketed recouplings than the unbracketed versions. In practice, we found $\tau_{\mathrm{mix,opt}} = 200$ and 400 μs, for $[\mathrm{SR}2_2^1]/[\mathrm{BR}2_2^1]$ and $\mathrm{SR}2_2^1/\mathrm{BR}2_2^1$, respectively (not shown). This faster build-up during bracketed recoupling is also observed in simulations (Fig.S8). It must be noted that these mixing times are much smaller than for SQ-SQ experiments.

In Fig.7, we compare the robustness to offset and rf field of the three most efficient recoupling: $[\mathrm{SR}2_2^1]$, $\mathrm{BR}2_2^1$ and $[\mathrm{BR}2_2^1]$.

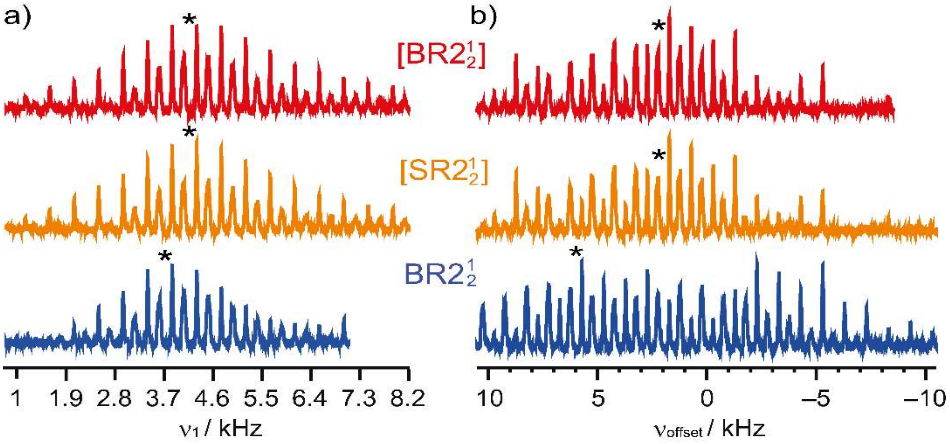

Fig.7. Experimental 1D ^{11}B DQ-filtered signal of $\mathrm{Li_2B_4O_7}$ corresponding to the first row ($t_1 = 0$) of DQ-SQ *D*-HOMCOR experiment using $[\mathrm{SR}2_2^1]$, $[\mathrm{BR}2_2^1]$ and $\mathrm{BR}2_2^1$ recoupling versus (a) ν_1 and (b) ν_{offset}. The $\mathrm{SR}2_2^1$ scheme is not shown because it is much less efficient than these three schemes (Fig.8). The optimum values are indicated with *. Each 1D spectrum results from averaging *NS* = 64 transients with $\tau_{\mathrm{RD}} = 1$ s.

The spectra shown in Fig.7a indicate that the experimental optimum rf-fields are slightly smaller than the theoretical value of $\nu_1 = 5$ kHz (Eq.1). This is due to the fact the transmitter must be applied off resonance from each peak. Therefore, the offset is added to the transverse rf-field (ν_1), which significantly increases the total nutation frequency. Moreover, the two bracketed schemes exhibit similar robustness to rf inhomogeneity, whereas the unbracketed one is more sensitive to deviation of the rf field from its optimum value. Conversely, $\mathrm{BR}2_2^1$ recoupling benefits from the highest robustness to offset, whereas $[\mathrm{SR}2_2^1]$ and $[\mathrm{BR}2_2^1]$ exhibit similar robustness to offset. Furthermore, the optimum offset values are equal to ca. 2 and 6 kHz (7.8 and 23.4 ppm) for the bracketed and un-bracketed versions, respectively, which means in the middle of the two resonances in the first case and off-resonance in the second case. The drop in DQ efficiency at the center of the two resonances for the $\mathrm{BR}2_2^1$ recoupling stems the contribution of offset to the reintroduction of the homonuclear dipolar coupling (Eq.5).

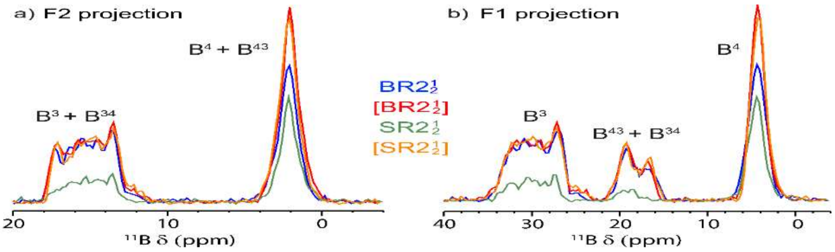

Fig.8. (a) F_2 and (b) F_1 sum projections of 2D ^{11}B DQ-SQ *D*-HOMCOR spectra of $Li_2B_4O_7$ using [SR2^1_2], [BR2^1_2], SR2^1_2 and BR2^1_2 recouplings recorded at 18.8 T with ν_R = 20 kHz. The 2D spectra were acquired using NUS retaining 33% of the points with respect to uniform sampling. The 2D spectra resulted from averaging *NS* = 64 transients for each of N_1 = 120 t_1-increment with a recovery delay τ_{RD} = 1 s, yielding an experimental time $T_{exp} \approx$ 43 min. The rf amplitude during the recoupling was equal to ν_1 = 3.7 and 4.1 kHz for BR2^1_2 / SR2^1_2 and [BR2^1_2] / [SR2^1_2], respectively.

Fig.S6a shows the 2D DQ-SQ *D*-HOMCOR spectrum of $Li_2B_4O_7$ acquired using the BR2^1_2 recoupling. This spectrum displays two cross-peaks B^{34} and B^{43} showing the spatial proximity between B_1^{III} and B^{IV} sites. This proximity was already observed in 2D ^{11}B SQ-SQ *D*-HOMCOR spectra. However, the presence of autocorrelation B^3 and B^4 peaks also indicates that B^{III} and B^{IV} sites are close to other B^{III} and B^{IV} sites, respectively. Fig.8 presents a comparison of the F_1 and F_2 projections of the 2D DQ-SQ *D*-HOMCOR spectra of $Li_2B_4O_7$ acquired with the four different recoupling sequences. The two bracketed recoupling sequences yield the highest intensities for all the signals. The B^4 autocorrelation peak is less intense when using the BR2^1_2 recoupling, while the intensities of the other peaks remain similar to those achieved using [SR2^1_2] and [BR2^1_2]. The SR2^1_2 recoupling is much less efficient than the other schemes.

IV.1.c. Comparison of SQ-SQ and DQ-SQ results

Fig.9 compares the slices along the F_2 dimension of 2D ^{11}B *D*-HOMCOR spectra using SQ-SQ with (SR2^1_2)$_4$ and DQ-SQ with [BR2^1_2], [SR2^1_2] and BR2^1_2. The 2D DQ-SQ spectra were sheared by a factor of two so that they can be displayed with the same scales along the F1 dimension as the SQ-SQ spectrum (Fig.S6b).

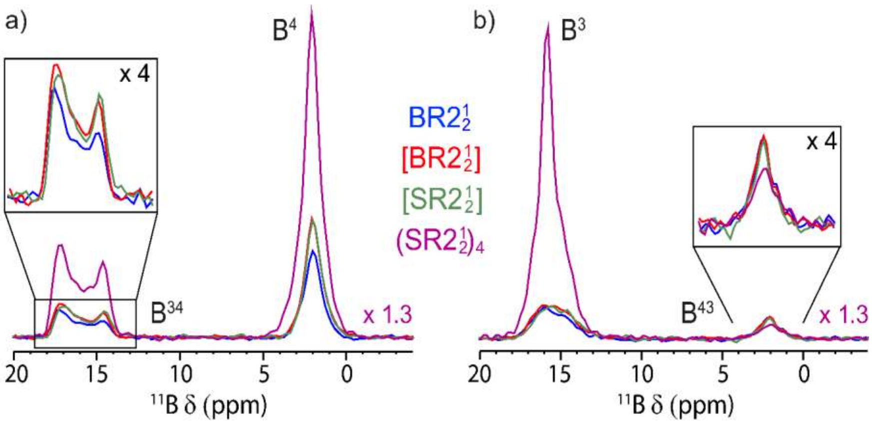

Fig.9. Comparison of 1D slices of $Li_2B_4O_7$ acquired at 18.8 T with ν_R = 20 kHz along the F_2 dimension corresponding to (a) B^4 diagonal peak and B^{34} cross-peak and (b) B^3 diagonal peak and B^{43} cross-peak of 2D ^{11}B *D*-HOMCOR spectra using SQ-SQ with (SR2^1_2)$_4$ and sheared DQ-SQ with [BR2^1_2], [SR2^1_2] and BR2^1_2. An expansion of the cross-peaks is also shown. The SQ-SQ spectrum was acquired with τ_{mix} = 3.2 ms and ν_{offset} = 3 kHz. The other experimental parameters for the acquisition of this spectrum are given in the caption of Fig.3, whereas those used to record DQ-SQ spectra are indicated in the caption of Fig.8. The intensities of the slices were normalized with respect to the *NS* values.

This comparison shows that the SQ-SQ spectrum using the (SR2^1_2)$_4$ recoupling exhibits a B^{34} cross-peak with a two-fold higher intensity than the DQ-SQ counterparts, but that its B^{43} cross-peak is less intense than for DQ-SQ spectra. This difference stems from the much faster decay of SQ coherences of $^{11}B^{III}$ nuclei with respect to $^{11}B^{IV}$. The B^3 and B^4 autocorrelation peaks are more intense in the SQ-SQ variant, but they do not provide information on ^{11}B-^{11}B proximities, contrary to those detected in the DQ-SQ spectra.

As a conclusion for spin-3/2 nuclei with small or moderate CSAs and chemical shift differences, such as ^{11}B, the DQ-SQ sequences using $[BR2_2^1]$ and $[SR2_2^1]$ bracketed recouplings represent the best choice since they provide information on the nuclei with close or identical resonance frequencies, while providing good efficiency.

IV.2. ^{27}Al-^{27}Al *D*-HOMCOR of AlPO$_4$-14.

^{27}Al is a spin-5/2 isotope with a natural abundance of 100% and a Larmor frequency of $\nu_0 = 208.6$ MHz at 18.8 T. ^{27}Al NMR spectra exhibit a larger chemical shift range than ^{11}B. As an example, the chemical shift difference between tetra- (Al^{IV}) and hexa-coordinated (Al^{VI}) aluminum nuclei is approximately 2.5 times larger than that between ^{11}B^{III} and ^{11}B^{IV} nuclei and reaches $\Delta \approx 10$ kHz at 18.8 T. For such large Δ value, $(SR2_2^1)$ and $(SR2_4^1)$ recouplings have been recommended for the acquisition of 2D SQ-SQ *D*-HOMCOR spectra [17,18]. Therefore, we will compare hereafter the performances of SQ-SQ *D*-HOMCOR experiments using $(SR2_2^1)$ and $(SR2_4^1)$ recouplings and the DQ-SQ variant using $[BR2_2^1]$ and $BR2_2^1$ recouplings.

This comparison will be done for AlPO$_4$-14, which contains four crystallographically inequivalent aluminum species: two tetra- (Al_1^{IV} and Al_2^{IV}), one penta- (Al^{V}) and one hexa-coordinated (Al^{VI}) sites with the following NMR parameter (δ_{iso} (ppm), C_Q (MHz), η_Q) = (42.7, 1.72, 0.57), (43.5, 3.90, 0.83), (27.1, 5.61, 0.93) and (-1.3, 2.55, 0.67), respectively [32]. The diagonal peaks of Al_1^{IV} and Al_2^{IV} are not resolved in the recorded spectra. The diagonal peaks are labeled as Al^{j} with *j* the coordination number of Al atoms. The cross-peaks are labeled as Al^{jk}, where *j* and *k* denote the coordination number of the correlated ^{27}Al signals in F$_2$ and F$_1$ dimensions, respectively. Moreover, our sample contained an extra framework aluminum impurity at ca. 10 ppm indicated with a star in Figs.**10**,**12** and **13**.

IV.2.a. SQ-SQ

Fig.**10** shows the 2D SQ-SQ spectrum of AlPO$_4$-14 recorded using the $(SR2_4^1)_4$ recoupling. All cross-peaks are observed, even the Al^{46} and Al^{64} ones corresponding to a difference in isotropic chemical shifts of 10 kHz and a small dipolar coupling of $|b_{IV\text{-}VI}|/(2\pi) = 52$ Hz related to the long inter-nuclear distance of 5.4 Å.

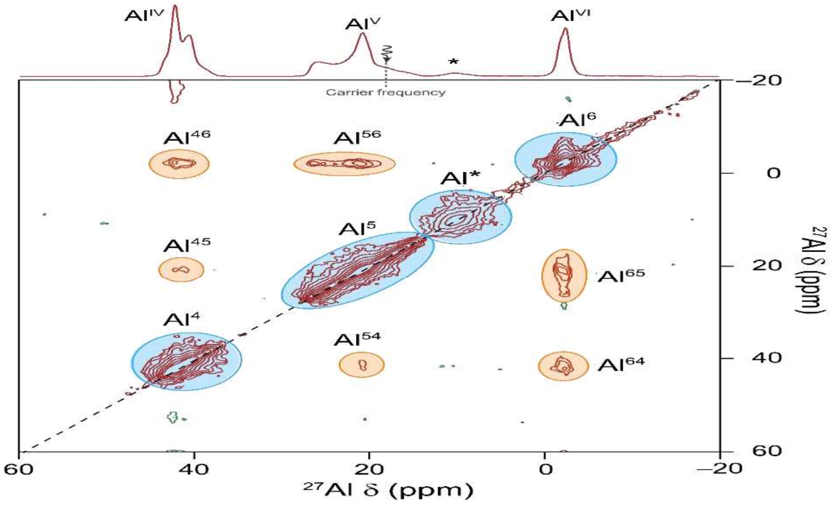

Fig.10. 2D ^{27}Al SQ-SQ *D*-HOMCOR spectrum of AlPO$_4$-14 using $(SR2_4^1)$ recoupling acquired at 18.8 T with $\nu_R = 20$ kHz. The 2D spectrum was recorded using NUS retaining 33% of the points with respect to uniform sampling. Cross- and auto-correlation peaks are circled with orange and blue ovals, respectively. The extra framework impurity at 10 ppm is indicated with a star. The 2D spectrum results from averaging $NS = 48$ transients for each of $N_1 = 330$ t_1-increment with a recovery delay $\tau_{RD} = 1$ s, yielding an experimental time $T_{exp} \approx 90$ min. The rf-amplitude during the recoupling was equal to $\nu_1 = 2.4$ kHz, whereas the offset was equal to $\nu_{offset} = 4$ kHz (19.2 ppm). The length of recoupling is $\tau_{mix} = 3.2$ ms.

As seen in Fig.11, the intensity of the cross-peaks represents only a few percent of that of the diagonal peaks, which do not provide information on the proximities. The intensities of the cross-peaks are similar for the two recoupling schemes.

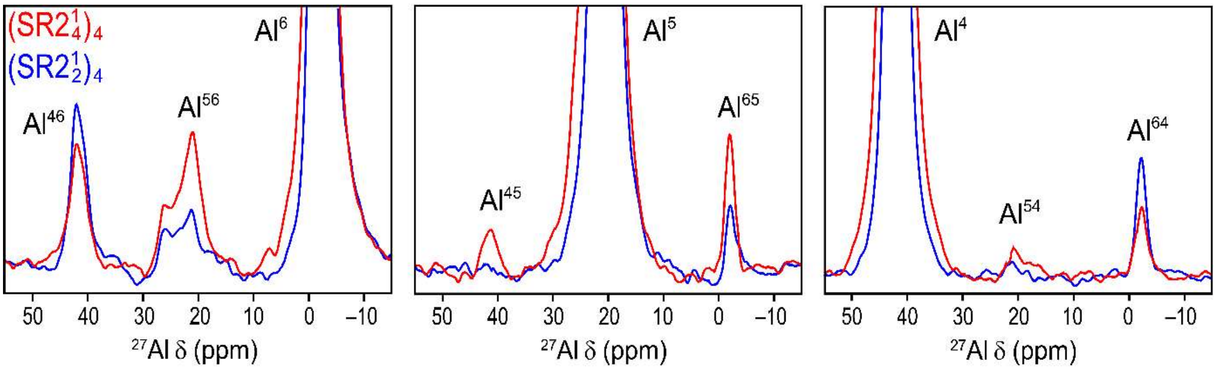

Fig.11. Comparison of 1D slides along F$_2$ dimension of 2D ^{27}Al SQ-SQ *D*-HOMCOR spectra of AlPO$_4$-14 using (SR2$^1_2$) and (SR2$^1_4$)$_4$ recouplings acquired at 18.8 T and ν_R = 20 kHz. The diagonal peaks, which are not informative, are truncated. The length of recoupling is τ_{mix} = 4.8 ms and ν_{offset} = 2.82 kHz (13.5 ppm). The other experimental parameters are given in the caption of Fig.10.

IV.2.b. DQ-SQ

As seen in Fig.12, the 2D ^{27}Al DQ-SQ spectrum is dominated by four resonances: the two autocorrelation peaks Al^6 and Al^4 corresponding to Al^{VI}-Al^{VI} distance of 2.9 Å, *i.e.* $|b_{VI\text{-}VI}|/(2\pi)$ = 333 Hz and Al$^{IV}_1$-Al$^{IV}_2$distances ranging from 4.3 to 4.8 Å, *i.e.* $73 \leq |b_{IV,1\text{-}IV,2}|/(2\pi) \leq 102$ Hz as well as the Al^{56} and Al^{65} cross-peaks corresponding to Al^V-Al^{VI} distance of 3.6 Å, *i.e.* $|b_{V\text{-}VI}|/(2\pi)$ = 174 Hz. The two other pairs of cross-peaks Al^{46}/Al^{64} and Al^{45}/Al^{54} are also detected. The only missing correlation is the Al^5 autocorrelation peak since the distance between the closest Al^V sites in AlPO$_4$-14 is equal to 6.7 Å, *i.e.* a small dipolar coupling constant $|b_{V\text{-}V}|/2\pi$ = 27 Hz. Owing to this broad distribution of ^{27}Al-^{27}Al dipolar coupling constants between the different sites, the relative intensities of the correlation peaks strongly depends on the recoupling time. Here, the recoupling was chosen to optimize the intensity of the correlation peaks (Al^6, Al^{56}, Al^{65} and Al^4) corresponding to the shortest ^{27}Al-^{27}Al distances.

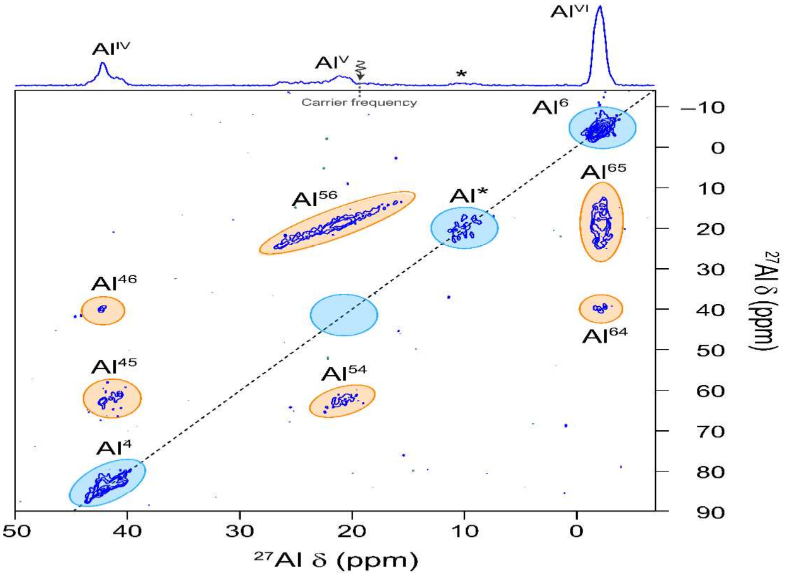

Fig.12. 2D ^{27}Al DQ-SQ *D*-HOMCOR spectrum of AlPO$_4$-14 using BR2$^1_2$ recoupling, acquired at 18.8 T and ν_R = 20 kHz. The 2D spectrum was acquired using NUS retaining 33% of the points with respect to uniform sampling. Cross- and autocorrelation peaks are circled with orange and blue ovals, respectively. The 2D spectrum results from averaging *NS* = 64 transients for each of N_1 = 330 t_1-increment with a recovery delay τ_{RD} = 1 s, yielding an experimental time $T_{exp} \approx$ 120 min. The rf amplitude during the recoupling was equal to ν_1 = 2.9 kHz, with ν_{offset} = 4 kHz (19.2 ppm). The length of recoupling is τ_{mix} = 0.8 ms.

As seen in Fig.13, the relative intensities of the correlation peaks are highly dependent on the offset as expected from Eq.5. Nevertheless, Fig.14b shows that the $\mathrm{BR}2_2^1$ recoupling is much more robust to offset than $[\mathrm{BR}2_2^1]$, as already noticed for ^{11}B isotope. The $\mathrm{BR}2_2^1$ recoupling is also more efficient than the bracketed variant for this sample, even if it is less robust to rf-inhomogeneity, as seen in Fig.14a.

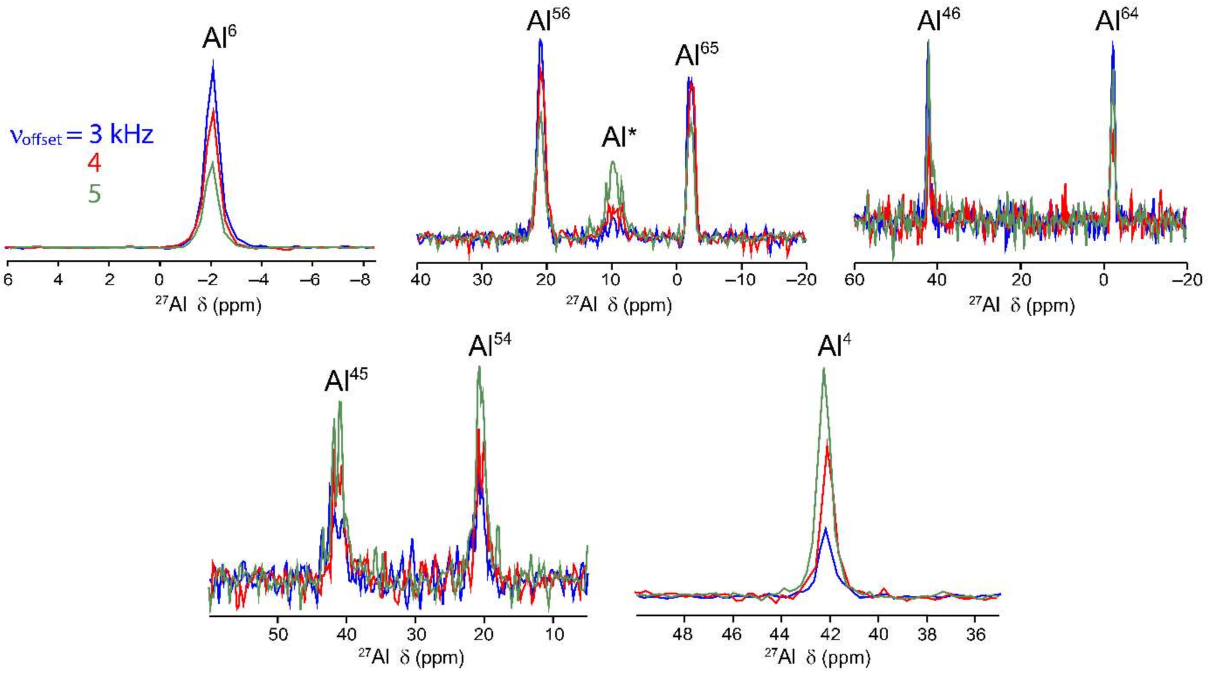

Fig.13. Comparison of 1D slides along the F$_2$ dimension of 2D ^{27}Al DQ-SQ *D*-HOMCOR spectra of AlPO$_4$-14 using $\mathrm{BR}2_2^1$ recoupling acquired at 18.8 T with ν_R = 20 kHz and ν_{offset} = 3, 4 or 5 kHz. The other experimental parameters are given in the caption of Fig.12.

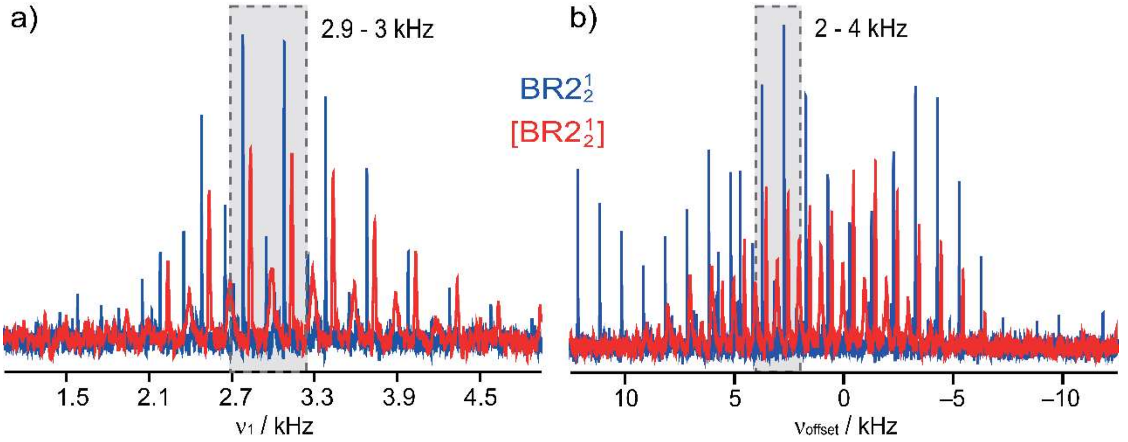

Fig.14. Experimental 1D ^{27}Al DQ-filtered signal of AlPO$_4$-14 corresponding to the first row (t_1 = 0) of DQ-SQ *D*-HOMCOR experiment using $[\mathrm{BR}2_2^1]$ (red) and $\mathrm{BR}2_2^1$ (blue) recouplings versus (a) ν_1 with ν_{offset} = 3 kHz and (b) ν_{offset} with ν_1 = 2.9 kHz. Each 1D spectrum results from averaging *NS* = 64 transients with a recovery delay τ_{RD} = 1 s. The length of recoupling is τ_{mix} = 0.4 ms. The rectangle with dashed frame indicates the optimal ν_1 and ν_{offset} values in each panel.

IV.2.c. Comparison of SQ-SQ and DQ-SQ results

Fig.15 compares the 1D slices along the F$_2$ dimension of 2D ^{27}Al SQ-SQ and sheared DQ-SQ *D*-HOMCOR spectra of AlPO$_4$-14 using $(\mathrm{SR}2_4^1)_4$ and $\mathrm{BR}2_2^1$ schemes, respectively. The low intensity of the cross-peaks compared to the diagonal peaks of SQ-SQ spectra demonstrates the poor efficiency of the *D*-HOMCOR sequences in the case of spin-5/2 nuclei, even in the case of small chemical shift differences, such as for Al^{56} and Al^{65} cross-peaks. This low efficiency has already been evidenced by numerical simulations of spin dynamics [19]. The lower signal-to-noise ratio compared to previously reported spectra acquired with the same NMR magnet on the same sample [16] stems from (i) the use of a smaller diameter rotor (3.2 instead of 4 mm) and (ii) the lack of schemes to enhance the CT population by manipulating the STs at the beginning of the sequence. Although the use of 3.2 mm rotors reduces the sensitivity, it allows the use of faster MAS frequencies, thus increasing the width of the indirect spectral dimension and improving the robustness to offset [16].

Furthermore, Fig.15 shows that the DQ-SQ experiment using the $\mathrm{BR}2_2^1$ scheme yields cross-peaks with intensities larger than or equal to those observed for the SQ-SQ variant using $(\mathrm{SR}2_4^1)_4$ recoupling. Therefore, for ^{27}Al isotope, the DQ-SQ technique based on $\mathrm{BR}2_2^1$ recoupling is recommended since it is more efficient and allows the observation of proximities between nuclei with close or identical frequencies.

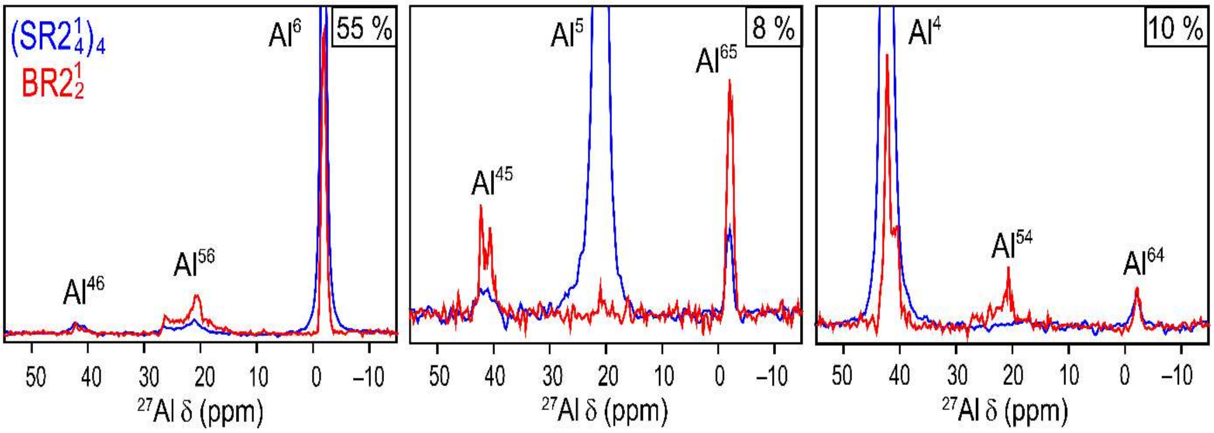

Fig.15. Comparison of 1D slices along the F_2 dimension of ^{27}Al *D*-HOMCOR 2D spectra of $\mathrm{AlPO_4}$-14 at 18.8 T with $\nu_R = 20$ kHz corresponding to (a) Al^6 , (b) Al^5 and (c) Al^4 diagonal peaks of SQ-SQ spectrum with $(\mathrm{SR}2_4^1)_4$ recoupling and sheared DQ-SQ counterpart with $\mathrm{BR}2_2^1$. The experimental parameters for the acquisition of the SQ-SQ spectrum are given in the caption of Fig.10, whereas those used to record DQ-SQ spectra are indicated in the caption of Fig.12. The intensities of slices were normalized with respect to the *NS* values. The diagonal peaks, which are not informative, are truncated.

IV. Conclusion

We have analyzed and compared the performances of SQ-SQ and DQ-SQ *D*-HOMCOR experiments for half-integer spin quadrupolar nuclei subject to small or moderate CSA, namely ^{11}B and ^{27}Al. For both isotopes, we recommend the DQ-SQ sequences, which allow the observation of proximities between nuclei with close or identical resonance frequencies and are more efficient than the SQ-SQ variants for ^{27}Al nuclei. We employed recoupling sequences based on the HORROR condition, with an rf amplitude slightly smaller than the theoretical one, $\nu_R/(2I + 1)$, owing to offsets, which slightly increase the nutation frequency.

For ^{11}B nuclei, which usually exhibit small or moderate differences in isotropic chemical shifts (≤ 5 kHz at 18.8 T), we recommend the $[\mathrm{SR}2_2^1]$ or $[\mathrm{BR}2_2^1]$ schemes, whereas for ^{27}Al isotope, for which the differences in isotropic chemical shifts are larger and can reach 10 kHz at 18.8 T, the $\mathrm{BR}2_2^1$ recoupling, which is more robust to offset, is recommended. Nevertheless, the case of half-integer spin quadrupolar nuclei subject to large CSA, e.g. ^{17}O at very high magnetic fields, was not investigated here. Large CSA can decrease the efficiency of these recoupling schemes.

A limitation of these *D*-HOMCOR experiments is their low transfer efficiency, notably for high spin values, owing to the difficulty to control the coherence transfer in large density matrices of quadrupolar nuclei. The sensitivity can be enhanced by (i) the irradiation of the STs at the beginning of the sequence to enhance the population difference across the CT [16] and (ii) the use of dynamic nuclear polarization (DNP) under MAS conditions [33]. Furthermore, the acquisition of these 2D experiments can be accelerated by using non-uniform sampling (NUS) [26,27,34], a covariance data treatment [35], or both [36]. In particular, we have introduced adequate covariance data treatment of DQ-SQ spectra, in which diagonal peaks are added before being subtracted since covariance treatments require the magnitudes of the diagonal peaks to be larger than those of the cross-peaks [37].

Acknowledgments

This article is dedicated to Dr. Francis Taulelle, our friend, who passed away recently and who contributed to the development of through-space homonuclear correlation for half-integer spin quadrupolar nuclei. The Chevreul Institute (FR 2638), Ministère de l'Enseignement Supérieur, de la Recherche et de l'Innovation, Hauts-de-France Region, and FEDER are acknowledged for supporting and funding partially this work. Financial support from the IR-RMN-THC FR-3050 CNRS for conducting the research is gratefully acknowledged. This project has received funding from the European Union's Horizon 2020 research and innovation program under grant agreement No. 731019 (EUSMI). OL acknowledges financial support from contract ANR-18-CE08-0015-01 (ThinGlass). FP acknowledges financial support from I-site contract OPE-2019-0043 (5400-MOFFIN).

References

[1] S.E. Ashbrook, S. Sneddon, New Methods and Applications in Solid-State NMR Spectroscopy of Quadrupolar Nuclei, *J. Am. Chem. Soc*. 136 (**2014**) 15440–15456. https://doi.org/10.1021/ja504734p.

[2] S. Ding, C.A. McDowell, Spectral spin diffusion of a spin-3/2 system in rotating solids, *Molec. Phys*. 85 (**1995**) 283–298. https://doi.org/10.1080/00268979500101111.

[3] N.G. Dowell, S.E. Ashbrook, S. Wimperis, Relative Orientation of Quadrupole Tensors from High-Resolution NMR of Powdered Solids, *J. Phys. Chem*. A. 106 (**2002**) 9470–9478. https://doi.org/10.1021/jp021315z.

[4] M.J. Duer, Determination of structural data from multiple-quantum magic-angle spinning NMR experiments, *Chem. Phys. Lett*. 277 (**1997**) 167–174.

[5] M.J. Duer, A.J. Painter, Correlating quadrupolar nuclear spins : a multiple-quantum NMR approach, *Chem. Phys. Lett*, 313 (**1999**) 763–770.

[6] M. Edén, L. Frydman, Quadrupolar-driven recoupling of homonuclear dipolar interactions in the nuclear magnetic resonance of rotating solids, *J. Chem. Phys*. 114 (**2001**) 4116. https://doi.org/10.1063/1.1344886.

[7] M. Edén, L. Frydman, Homonuclear NMR Correlations between Half-Integer Quadrupolar Nuclei Undergoing Magic-Angle Spinning, *J. Phys. Chem. B*. 107 (**2003**) 14598–14611. https://doi.org/10.1021/jp035794t.

[8] M. Nijman, M. Ernst, A.P.M. Kentgens, B.H. Meier, Rotational-resonance NMR experiments in half-integer quadrupolar spin systems, *Molec. Phys*. 98 (**2000**) 161–178. https://doi.org/10.1080/00268970009483280.

[9] M. Baldus, D. Rovnyak, R.G. Griffin, Radio-frequency-mediated dipolar recoupling among half-integer quadrupolar spins, *J. Chem. Phys*. 112 (**2000**) 5902–5909. https://doi.org/10.1063/1.481187.

[10] A.J. Painter, M.J. Duer, Double-quantum-filtered nuclear magnetic resonance spectroscopy applied to quadrupolar nuclei in solids, *J. Chem. Phys*. 116 (**2002**) 710–722. https://doi.org/10.1063/1.1425831.

[11] S. Wi, J.W. Logan, D. Sakellariou, J.D. Walls, A. Pines, Rotary resonance recoupling for half-integer quadrupolar nuclei in solid-state nuclear magnetic resonance spectroscopy, *J. Chem. Phys*. 117 (**2002**) 7024–7033. https://doi.org/10.1063/1.1506907.

[12] G. Mali, G. Fink, F. Taulelle, Double-quantum homonuclear correlation magic angle sample spinning nuclear magnetic resonance spectroscopy of dipolar-coupled quadrupolar nuclei, *J. Chem. Phys*. 120 (**2004**) 2835–2845. https://doi.org/10.1063/1.1638741.

[13] M. Edén, H. Annersten, A. Zazzi, Pulse-assisted homonuclear dipolar recoupling of half-integer quadrupolar spins in magic-angle spinning NMR, *Chem. Phys. Lett*. 410 (**2005**) 24–30. https://doi.org/10.1016/j.cplett.2005.04.030.

[14] M. Edén, D. Zhou, J. Yu, Improved double-quantum NMR correlation spectroscopy of dipolar-coupled quadrupolar spins, *Chem. Phys. Lett*. 431 (**2006**) 397–403. https://doi.org/10.1016/j.cplett.2006.09.081.

[15] A.Y.H. Lo, M. Edén, Efficient symmetry-based homonuclear dipolar recoupling of quadrupolar spins: double-quantum NMR correlations in amorphous solids, *Phys. Chem. Chem. Phys*. 10 (**2008**) 6635–6644. https://doi.org/10.1039/B808295B.

[16] Q. Wang, B. Hu, O. Lafon, J. Trébosc, F. Deng, J.-P. Amoureux, Double-quantum homonuclear NMR correlation spectroscopy of quadrupolar nuclei subjected to magic-angle spinning and high magnetic field, *J. Magn. Reson.* 200 (**2009**) 251–260. https://doi.org/10.1016/j.jmr.2009.07.009.

[17] Y. Yu, P. Keil, B. Stevensson, M.R. Hansen, M. Edén, Assessment of new symmetry-based dipolar recoupling schemes for homonuclear magnetization exchange between quadrupolar nuclei in two-dimensional correlation MAS NMR, *J. Magn. Reson.* 316 (**2020**) 106734. https://doi.org/10.1016/j.jmr.2020.106734.

[18] Y. Yu, P. Keil, M.R. Hansen, M. Edén, Improved Magnetization Transfers among Quadrupolar Nuclei in Two-Dimensional Homonuclear Correlation NMR Experiments Applied to Inorganic Network Structures, *Molecules.* 25 (**2020**) 337. https://doi.org/10.3390/molecules25020337.

[19] N.T. Duong, D. Lee, F. Mentink-Vigier, O. Lafon, G.D. Paëpe, On the use of radio-frequency offsets for improving double-quantum homonuclear dipolar recoupling of half-integer-spin quadrupolar nuclei, *Magn. Reson. Chem.* 59 (**2021**) 991–1008.

[20] M. Edén, A.Y.H. Lo, Supercycled symmetry-based double-quantum dipolar recoupling of quadrupolar spins in MAS NMR: I. Theory, *J. Magn. Reson.* 200 (**2009**) 267–279. https://doi.org/10.1016/j.jmr.2009.07.007.

[21] M. Edén, Recent Progress in Homonuclear Correlation Spectroscopy of Quadrupolar Nuclei, in: G.A. Webb (Ed.), *Modern Magnetic Resonance*, Springer International Publishing, Cham, **2017**: pp. 1–33. https://doi.org/10.1007/978-3-319-28275-6_104-1.

[22] G. Pileio, M. Concistrè, N. McLean, A. Gansmüller, R.C.D. Brown, M.H. Levitt, Analytical theory of γ-encoded double-quantum recoupling sequences in solid-state nuclear magnetic resonance, *J. Magn. Reson.* 186 (**2007**) 65–74. https://doi.org/10.1016/j.jmr.2007.01.009.

[23] C. Martineau, B. Bouchevreau, F. Taulelle, J. Trébosc, O. Lafon, J.-P. Amoureux, High-resolution through-space correlations between spin-1/2 and half-integer quadrupolar nuclei using the MQ-D-R-INEPT NMR experiment., *Phys. Chem. Chem. Phys.* 14 (**2012**) 7112–7119. https://doi.org/10.1039/c2cp40344g.

[24] Q. Wang, B. Hu, O. Lafon, J. Trébosc, F. Deng, J.-P. Amoureux, Homonuclear dipolar recoupling under ultra-fast magic-angle spinning: probing 19F-19F proximities by solid-state NMR, *J. Magn. Reson.* 203 (**2010**) 113–28. https://doi.org/10.1016/j.jmr.2009.12.00.

[25] S. Antonijevic, S.E. Ashbrook, S. Biedasek, R.I. Walton, S. Wimperis, H. Yang, Dynamics on the Microsecond Timescale in Microporous Aluminophosphate AlPO-14 as Evidenced by 27Al MQMAS and STMAS NMR Spectroscopy, *J. Am. Chem. Soc.* 128 (**2006**) 8054–8062. https://doi.org/10.1021/ja057682g.

[26] A. Sasaki, J. Trébosc, J.-P. Amoureux, A comparison of through-space population transfers from half-integer spin quadrupolar nuclei to ^{1}H using MQ-HETCOR and MQ-SPAM-HETCOR under fast MAS, *J. Magn. Reson.* 329 (**2021**) 107028. https://doi.org/10.1016/j.jmr.2021.107028.

[27] A. Sasaki, J. Trébosc, J.-P. Amoureux, Accelerating the acquisition of high-resolution quadrupolar MQ/ST-HETCOR 2D spectra under fast MAS via ^{1}H detection and through-space population transfers, *J. Magn. Reson.* 333 (**2021**) 107093. https://doi.org/10.1016/j.jmr.2021.107093.

[28] N.S. Barrow, J.R. Yates, S.A. Feller, D. Holland, S.E. Ashbrook, P. Hodgkinson, S.P. Brown, Towards homonuclear J solid-state NMR correlation experiments for half-integer quadrupolar nuclei: experimental and simulated ^{11}B MAS spin-echo dephasing and calculated $^{2}J_{BB}$ coupling constants for lithium diborate, *Phys. Chem. Chem. Phys.* 13 (**2011**) 5778. https://doi.org/10.1039/c0cp02343d.

[29] A. Kirfel, G. Will, R.F. Stewart, The chemical bonding in lithium metaborate, $LiBO_2$. Charge densities and electrostatic properties, *Acta Crystallogr B Struct Sci.* 39 (**1983**) 175–185. https://doi.org/10.1107/S0108768183002256.

[30] L.S. Vorotilova, L.V. Dmitrieva, A.V. Samoson, NMR spectral study of two crystalline modifications of lithium metaborate, $LiBO_2$, *J. Struct. Chem.* 30 (**1989**) 756–759. https://doi.org/10.1007/BF00763796.

[31] A. Kuhn, E. Tobschall, P. Heitjans, Li Ion diffusion in nanocrystalline and nanoglassy $LiAISi_2O_6$ and $LiBO_2$ - Structure dynamics relations in two glass forming compounds, *Zeitschrift Für Physikalische Chemie.* 223 (**2009**) 1359–1377. https://doi.org/10.15488/2264.

[32] C. Fernandez, J.-P. Amoureux, J.M. Chezeau, L. Delmotte, H. Kessler, ^{27}Al MAS NMR characterization of $AlPO_4$ -14 enhanced resolution and information by MQMAS, *Microporous Materials*. 6 (**1996**) 331–340. https://doi.org/10.1016/0927-6513(96)00040-5.

[33] D. Lee, H. Takahashi, A.S. Lilly Thankamony, J.-P. Dacquin, M. Bardet, O. Lafon, G.D. Paëpe, Enhanced Solid-State NMR Correlation Spectroscopy of Quadrupolar Nuclei Using Dynamic Nuclear Polarization, *J. Am. Chem. Soc.* 134 (**2012**) 18491–18494. https://doi.org/10.1021/ja307755t.

[34] E.C. Lin, S.J. Opella, Sampling scheme and compressed sensing applied to solid-state NMR spectroscopy, *J. Magn. Reson*. 237 (**2013**) 40–48. https://doi.org/10.1016/j.jmr.2013.09.013.

[35] B. Hu, J.-P. Amoureux, J. Trébosc, M. Deschamps, G. Tricot, Solid-state NMR covariance of homonuclear correlation spectra, *J. Chem. Phys*. 128 (**2008**) 134502. https://doi.org/10.1063/1.2884341.

[36] Y. Li, B. Hu, Q. Chen, Q. Wang, Z. Zhang, J. Yang, I. Noda, J. Trébosc, O. Lafon, J.-P. Amoureux, F. Deng, Comparison of various sampling schemes and accumulation profiles in covariance spectroscopy with exponentially decaying 2D signals, *Analyst*, 138 (**2013**) 2411. https://doi.org/10.1039/c3an36375a.

[37] O. Lafon, B. Hu, J.-P. Amoureux, P. Lesot, Fast and High-Resolution Stereochemical Analysis by Nonuniform Sampling and Covariance Processing of Anisotropic Natural Abundance 2D 2H NMR Datasets, *Chem. Eur. J.* 17 (**2011**) 6716–6724. https://doi.org/10.1002/chem.201100461.